Transient response of a metallic capsule to an internal pressure pulse

Michael El-Raheb *

Wave Research, Applied Mechanics, 1000 Oak Forest Lane, Pasadena 91107, USA

Abstract

Response of a metallic capsule to a transient internal pressure is analyzed adopting two models. The first is a two-dimensional (2-D) model with finite extent in the plane of the capsule's cross-section and infinite length normal to that plane. The second is a three-dimensional (3-D) axisymmetric model consisting of a short thin cylinder capped by thin disks. In both models, transfer matrices relate state vectors of tractions and displacements at two segment boundaries. The time interval from pressure initiation to failure of its material measures the capsule's effectiveness as a confining boundary.

© 2004 Elsevier Ltd. All rights reserved.

Keyword: Wave propagation

1. Introduction

Ceramic materials are used to harden vehicles and structures against ballistic events. These materials benefit from a higher compressive strength compared to metals yet their tensile strength is reduced by brittle failure. Following impact, a ceramic material shocks the projectile initiating damage. As time progresses and tensile release waves form, micro-cracks propagate and multiply in the material culminating in total failure. Strain energy in the virgin material then converts into kinetic energy ejecting the debris away from the projectile's path. Prolonging the time interval when comminuted material remains in this path after failure is one way to extend the material's utility in eroding the projectile.

In what follows a quantitative account is given of an experimental project duplicated in two laboratories and aimed at evaluating ballistic performance of stacked configurations. This account is interesting as unplanned differences in experimental setups revealed the strong effect of confinement on penetration.

Controlled ballistic experiments on periodic stacks of ceramic layers bonded by thin polymer films were performed at two laboratories named "A" and "B" for shortness (Weber and Hohler, 1997;

---

* Tel.: +1-626-7965528; fax: +1-626-5838834.
E-mail address: mertrident@earthlink.net (M. El-Raheb).

Weber et al., 1999). Ballistic performance was measured by the residual penetration p_r of the projectile into a thick aluminum backing block. In this way p_r is a measure of the projectile's residual kinetic energy. All experiments consisted of stacks made of 100 mm × 100 mm square aluminum nitride (AlN) tiles and 38 mm total thickness of either: 1 × 38 mm monolith, 2 × 19 mm layers, 3 × 12.7 mm layers, or 6 × 6.35 mm layers. All layers were bonded by 0.254 mm uniform polyurethane film, adhering to the tiles by heating.

In **Series 3c**, the stacks in the "B" setup were confined laterally by 14 cm × 14 cm square steel tubing 12.5 mm thick, and axially by a 5 mm thick steel cover plate perforated centrally with a 30 mm diameter hole allowing the projectile to strike the stack (Fig. 1(a)). The stack rested on a 60 mm Aluminum backing block to serve as witness plate for p_r measurements. The "A" setup was laterally confined by welding four 6.35 mm plates along the edges to form a box keeping a 5 mm clearance around the stack, and covered by a 6.35 mm plate. The cylindrical projectile was made of Tungsten alloy with 8.33 mm diameter and length to diameter ratio of 6, weighing 50 g, with velocity near 1170 m/s. Fig. 1(b) plots p_r versus number of layers in the stack for all "A" and "B" stacks tested. In this figure, data from each series of experiments is labeled by a different symbol like ●, △, □, and ×. At first, results from "A" and "B" did not match. "A" measured $p_r = 30$ mm for the 1.5 in. monolith, and $p_r = 0$ mm for the 1/2 in. layer stack (● Fig. 1(b)). "B" measured $p_r = 0$ mm for the 38 mm monolith and 6 mm for the 12.7 mm layer stack (not shown in Fig. 1(b)). A review of the "A" experimental setup revealed that lateral confinement failed at the corner welds, ejecting the side plates laterally immediately following impact thus negating the effect of confinement. This confirmed that the principal cause for the substantially lower p_r in the "B" setup was the strong confinement that delayed
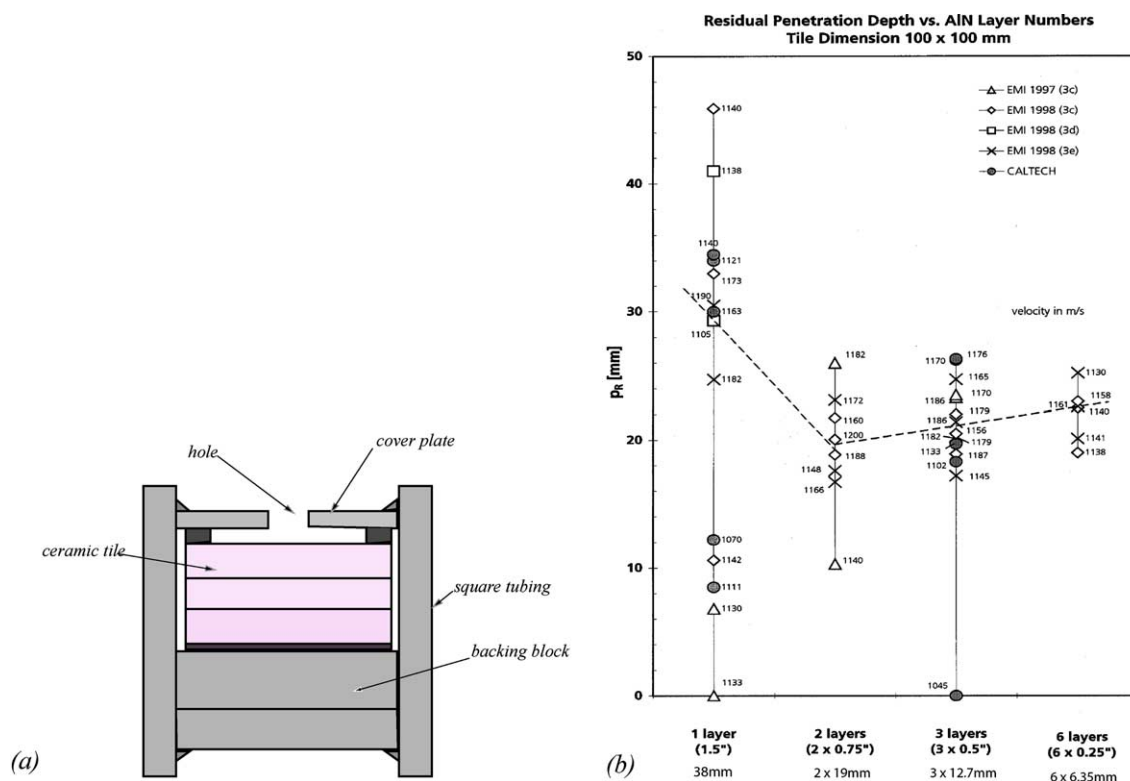

Fig. 1. Experiment: (a) setup, (b) residual penetration data.

removal of comminuted material from the projectile's path, increasing its erosion. This effect masked the real ballistic performance of ceramic.

The ''A'' and ''B'' setups repeated **Series 3c** experiments with the following changes. The size of the confining tube in ''B'' was increased allowing a 5 mm clearance around the stack for lateral expansion of the damaged ceramic without interference from the confining tube. Also, a 3 mm gap was left between cover plate and top face of the stack. In the ''A'' setup, the gap between stack, sidewalls and cover plate was increased to 20 mm practically eliminating the effect of confinement. Indeed, results for the 12.7 mm layer stack agreed: ''B'' measured $p_r = 20$ mm and 23 mm ($\triangle$ Fig. 1(b)), and ''A'' measured $p_r = 20$ mm and 26 mm ($\bullet$ Fig. 1(b)). For the 38 mm monolith the mismatch in p_r persisted: ''B'' measured $p_r = 6.8$ mm and 0 mm ($\triangle$) pointing to a possible problem in the ''B'' setup. ''B'' was repeated in three more tests on the 38 mm monolith yielding $p_r = 11$, 33 and 46 mm ($\diamond$ Fig. 1(b)). This unusual scatter among ''B'' results for the 38 mm monolith confirmed that a fundamental difference existed between the two setups meriting a closer look at the ''B'' setup. Examining the ''B'' cover plates of the last three tests revealed that the cover plate corresponding to $p_r = 11$ mm suffered substantial plastic deformation, while that corresponding to $p_r = 46$ mm had very little plastic deformation. This suggested that the large scatter in p_r was caused by how the cover plate confines ejecta in the direction of impact. The 3 mm gap between cover plate and stack in ''B'' was small enough to confine ejecta at times when they did not escape through the central hole in the cover plate remaining in the path of the projectile. This increased resistance, reducing p_r and creating sufficient pressure to cause the cover plate to yield. When ejecta escaped through the hole, the projectile encountered less resistance increasing p_r and keeping the cover plate intact. This demonstrated that even the weak confinement of the cover plate randomly affected ballistic performance by retaining or allowing ejecta to pass through the hole.

An explanation was still needed to account for the match in results and reduced scatter in the ''B'' data of **Series 3c** for the multiple layer configurations in spite of the cover plate's closeness. That explanation lies in the concept of phase velocity c_p. For the monolith, the rate of formation of comminuted material in ejecta is approximately the compression speed of sound, which for AlN is 10 km/s. For a stack made of 12.7 mm ceramic layers bonded by 0.254 mm polyurethane film, $c_p \sim \sqrt{(E_b h_c)/(\rho_c h_b)} = 1.7$ km/s where ρ_c, h_c are ceramic mass density and layer thickness, and E_b, h_b are film modulus and thickness (El-Raheb, 1997). The reduction in c_p caused by dispersion from weak coupling reduces the rate of ejecta formation by a factor of 6. This raises the probability of ejecta escaping from the hole and in turn diminishes scatter. In fact, the reduction in p_r scatter for stacks with thinner ceramic layers is consistent with the corresponding reduction in c_p.

To bring the two setups into equivalence required adjusting the ''B'' setup in **Series 3d** by increasing the distance between cover plate and stack from 3 to 50 mm. This allowed sufficient space for the ejecta to expand without restriction from confinement. With this final setup, experiments measured a higher p_r in two tests with the 38 mm monolith: 29 and 41 mm ($\square$ Fig. 1(b)). Faced with this unexpectedly strong effect of confinement, the confining tubing in the ''B'' setup was increased from 14 to 19.5 cm and two more tests were performed for each stack reducing the scatter to less than 15% in **Series 3e**. For the 38 mm monolith, $p_r = 25$ mm and 31 mm ($\times$ Fig. 1(b)).

Note the large scatter in p_r for the monolith when gap between cover plate and stack was 3 mm ($\triangle$ and $\diamond$ Fig. 1(b)), and the reduced scatter of all data when that gap was increased to 50 mm ($\square$ and $\times$ Fig. 1(b)). The scatter diminishes as layer thickness in the stack is reduced.

Examining the experimental results presented above, it is evident that metallic encapsulation of ceramic tiles may extend the time interval of active resistance against the projectile also known as dwell time. One drawback is added weight implying that an optimization process is needed to determine the appropriate material properties and thickness of the capsule wall for maximum specific performance (performance/weight ratio). One measure of increased performance is the time interval it takes from total comminuting of ceramic to failure of the capsule allowing confined comminuted material to extend projectile erosion.

This work focuses on the transient response of a hollow capsule excited internally by a time dependent pressure pulse. Two models of the capsule are developed:

(a) A 2-D model of four strips connected at the edges forming a hollow rectangle, with finite extent in the plane of the cross-section and infinite in the direction normal to it.
(b) A 3-D axisymmetric model of a short thin cylinder capped by thin disks at the cylinder's ends.

In the 2-D model, the transfer matrix approach is utilized to relate state vectors at the two ends of a 2-D strip. In the 3-D axisymmetric model, a transfer matrix is also used for the cylinder, while each disk is modeled as dynamic impedances relating force to displacement vectors along the boundary.

The internal pressure generated by the expanding comminuted material is approximated by a hyperbolic cosine bell-shaped distribution with origin at the center of the faceplates simulating peak pressure at impact and pressure decay remote from impact. This approximation is consistent with both a hydro-acoustic model of the comminuted material based on the small amplitude acoustic equation and a numerical distribution determined by "EPIC" a general purpose "hydrocode".

Presented in a forthcoming paper, the acoustic model for internal pressure requires the compliance of the capsule walls. An appropriate measure for compliance is dynamic mobility of the capsule that relates internal pressure to normal acceleration at the boundary. Dynamic mobility is derived from frequency response adopting the modal method.

Finally, a parametric analysis compares histories from the 2-D and 3-D models with emphasis on peak stress and its location. Also, frequency response of driving point mobility yields its frequency-averaged radial distribution serving as an input to the acoustic model for internal pressure.

Since the 3-D axisymmetric model combines disk and cylinder, a literature survey focuses on each component separately as analysis on structures combining both is rare as the preferred approach relies on general purpose computer programs.

A large body of references exists treating static and dynamic problems of isotropic, orthotropic, stiffened and rotating disks. A major portion concerns frequency response while a smaller portion treats transient response. Soamidas and Ganesan (1991) analyze variable thickness polar orthotropic disks. Xiang et al. (1996) treat linear axisymmetric frequency response with concentric stiffeners. Karunasena et al. (1997) treat the static axisymmetric response of a disk with annular supports adopting Mindlin's plate equations. Liew and Yang (2000) solve the three-dimensional free vibration problem of solid and annular plates for symmetric and asymmetric modes by an approximate polynomial-Ritz method. El-Raheb (1994b) and El-Raheb and Wagner (1987, 1994a) study the axisymmetric wave propagation in a disk from impulse of short duration adopting a plate flexural model and a 3-D elasticity model. El-Raheb and Wagner (2001) then extend the axisymmetric flexure model to asymmetric response from off-center impact.

For thin cylinders, Wang et al. (1997) utilize the Ritz method in the modal response of ring-stiffened cylinders. Um et al. (1998) derive 3-D elasticity solutions to frequency response of open cylinders. Lin and Jen (2003) adopt the Chebyshev collocation method in the analysis of laminated anisotropic cylinders. El-Raheb and Wagner (1989a) treat wave propagation in a thin cylinder with concentrated masses attached to its surface adopting a modal approach. El-Raheb and Wagner (1985, 1986, 1989b) adopt transfer matrices to treat frequency response of cylinders connected to toroidal shells stiffened by discrete rings and annular disks and damped by constrained visco-elastic layers applied to the surface.

2. 2-D model

Fig. 2(a) depicts the capsule geometry in the 2-D model. In this model, a rectangular plate with finite extent along the local x-axis and infinite length along the local z-axis is termed a 2-D strip. A schematic of
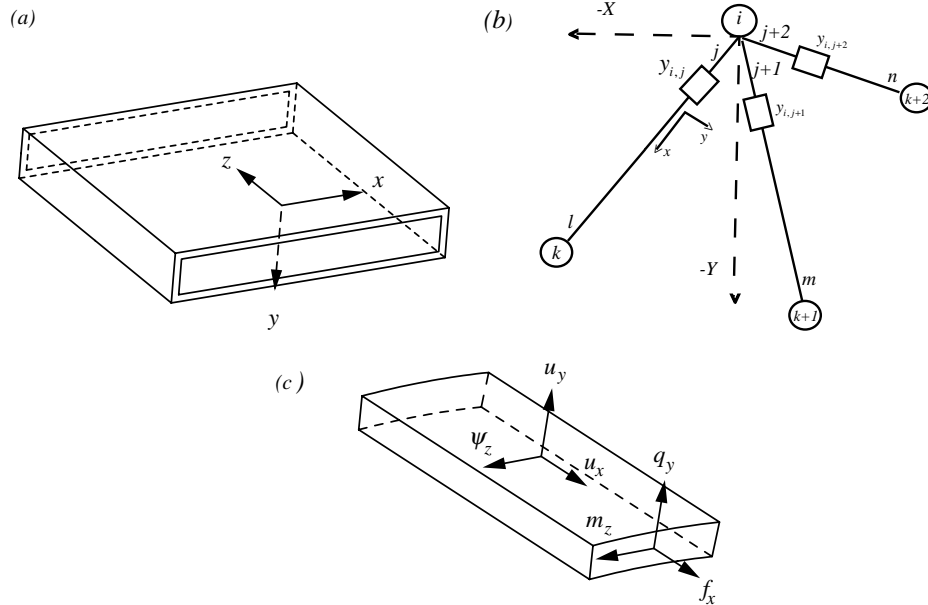
Fig. 2. 2-D model: (a) geometry, (b) corner-branch system, (c) strip element.

strips joining at corners through mobilities is shown in Fig. 2(b) where reference coordinate system (X, Y) is shown as dashed lines. Corner "i" (enclosed in a circle) joins three branches j, $j+1$ and $j+2$, through linkage mobilities $\mathbf{y}_{i,j}$, $\mathbf{y}_{i,j+1}$ and $\mathbf{y}_{i,j+2}$ respectively where (i,j) stands for the corner-branch dyad. In the frequency domain where time dependence is sinusoidal with frequency ω,

$$
\begin{aligned}
\mathbf{y}_{i,j} &= [\mathbf{z}_{i,j}]^{-1} \\
z_{i,j}^{(\alpha)} &= (-\hat{m}\omega^2 + \hat{k} + \mathrm{i}\omega\hat{\varsigma})_{i,j}^{(\alpha)}, \quad \alpha = 1, 2, \ \mathrm{i} = \sqrt{-1}
\end{aligned}
\tag{1}
$$

and $\mathbf{z}_{i,j}$ is a 2×2 diagonal impedance matrix with components the one-degree of freedom oscillators with mass $\hat{m}$, spring $\hat{k}$, viscous damper $\hat{\varsigma}$, along the local coordinates (x, y) of the jth branch. Let $\mathbf{A}_{i,j}$ be the 4×4 transformation matrix relating local to reference state vectors $\mathbf{S}^{\mathrm{loc}} \rightarrow \mathbf{S}^{\mathrm{ref}}$

$$
\mathbf{S}_{i,j}^{\mathrm{ref}} = \mathbf{A}_{i,j}\mathbf{S}_{i,j}^{\mathrm{loc}}, \quad \mathbf{S}_{i,j} = \{\mathbf{f}, \mathbf{g}\}_{i,j}^{\mathrm{T}}, \quad \mathbf{A}_{i,j} = \begin{bmatrix} \mathbf{a}_{i,j} & \mathbf{0} \\ \mathbf{0} & \mathbf{a}_{i,j} \end{bmatrix}
\tag{2}
$$

where $\{\mathbf{f}, \mathbf{g}\}_{i,j}^{\mathrm{T}}$ are force and displacement vectors at the end of branch (i,j) and $\mathbf{a}_{i,j}$ is the 2×2 transformation sub-matrix. Define $\mathbf{f}$ and $\mathbf{g}$ as

$$
\mathbf{f} = \{f_x, q_y, m_z\}^{\mathrm{T}}, \quad \mathbf{g} = \{u_x, u_y, \psi_z\}^{\mathrm{T}}
\tag{3}
$$

f_x, q_y, m_z are extensional force, shear force and moment, and u_x, u_y, ψ_z are corresponding displacements and rotation along local axes depicted in Fig. 2(c). Let $l_{i,j}$ be branch length then the state vector at $x = l_{i,j}$ is related to that at $x = 0$ by the transfer matrix

$$
\mathbf{S}_{i,j}(l) \equiv \left\{ \begin{array}{c} \mathbf{f}(l) \\ \mathbf{g}(l) \end{array} \right\}_{i,j} = \mathbf{T}_{i,j}(0 \rightarrow l)\mathbf{S}_{i,j}(0) \equiv \begin{bmatrix} \mathbf{t}_{11} & \mathbf{t}_{12} \\ \mathbf{t}_{21} & \mathbf{t}_{22} \end{bmatrix}_{i,j} \left\{ \begin{array}{c} \mathbf{f}(0) \\ \mathbf{g}(0) \end{array} \right\}_{i,j}
\tag{4}
$$

For a 2-D strip the transfer matrix is derived in Appendix A. Since linkage mobilities **y** and corner impedances **z** connect branch ends to rigid corners, $\tilde{\mathbf{S}}$ at a rigid corner is related to **S** at a branch end by

$$\left\{ \begin{array}{c} \tilde{\mathbf{f}} \\ \tilde{\mathbf{g}} \end{array} \right\}_{i,j} = \begin{bmatrix} \mathbf{I} & \mathbf{0} \\ \varepsilon_e \mathbf{y} & \mathbf{I} \end{bmatrix}_{i,j} \begin{bmatrix} \mathbf{I} & \varepsilon_e \mathbf{z} \\ \mathbf{0} & \mathbf{I} \end{bmatrix}_{i,j} \left\{ \begin{array}{c} \mathbf{f} \\ \mathbf{g} \end{array} \right\}_{i,j}, \quad \varepsilon_e = \left\{ \begin{array}{ll} 1 & \text{at } x = 0 \\ -1 & \text{at } x = l_{i,j} \end{array} \right. \tag{5}$$

At each corner, equilibrium of $\tilde{\mathbf{f}}$ and compatibility of $\tilde{\mathbf{g}}$ take the form

$$\sum_{j=1}^{n_{bi}} \mathbf{a}_{i,j} \tilde{\mathbf{f}}_{i,j} \varepsilon_e = \mathbf{0}, \quad i = 1, n_c$$
$$\mathbf{a}_{i,j} \tilde{\mathbf{g}}_{i,j} = \mathbf{a}_{i,1} \tilde{\mathbf{g}}_{i,1}, \quad j = 2, n_{bi}, \quad i = 1, n_c \tag{6}$$

where n_{bi} is number of branches joined at corner i and n_c is total number of corners. Substituting (5) in (6) and expressing $\mathbf{S}_{i,j}(l_{i,j})$ in terms of $\mathbf{S}_{l,j}(0)$ using (4) produces $6n_c$ simultaneous equations in the global $\mathbf{S}_G(0)$, the ensemble of all $\mathbf{S}_{i,j}(0)$ in the configuration

$$\mathbf{M}_G \mathbf{S}_G(0) = \mathbf{0}, \qquad \mathbf{S}_G(0) = \{\mathbf{S}_{i,j}(0)\}^{\mathrm{T}} \quad (j = 1, n_{bi}, i = 1, n_c) \tag{7}$$

Transient response is determined by modal analysis. The eigenset of (7) derives from

$$\det[\mathbf{M}_G] = \mathbf{0} \;\; \Rightarrow \;\; \{\mathbf{\Phi}; \boldsymbol{\omega}\}_k \tag{8}$$

$\{\mathbf{\Phi}; \boldsymbol{\omega}\}_k$ is the kth eigenset formed of the eigenvector

$$\mathbf{\Phi}_k = \{\varphi, \eta, \psi\}_k^{\mathrm{T}} \tag{8a}$$

and corresponding eigenvalue ω_k. The modal analysis proceeds by expanding the global displacement vector $\mathbf{g}_G(x, t)$ in terms of the orthogonal set (8a)

$$\mathbf{g}_G(x, t) = \sum_k b_k(t) \mathbf{\Phi}_k(x) \tag{9}$$

Substituting (9) in the forced elasto-dynamic equations of motion and enforcing orthogonality of the $\{\mathbf{\Phi}_k(x)\}$ set yields uncoupled ordinary differential equations in $b_k(t)$

$$\ddot{b}_k(t) + \omega_k^2 b_k(t) = N_{fk} f(t) / N_{kk}$$
$$N_{fk} = \langle \mathbf{p}(x) | \rho \mathbf{\Phi}_k(x) \rangle, \quad N_{kk} = \langle \mathbf{\Phi}_k(x) | \rho \mathbf{\Phi}_k(x) \rangle \tag{10}$$

($\dot{}$) is time derivative, $\mathbf{p}(x)$ is spatial vector of external excitation, $f(t)$ is its time dependence, and ρ is density. Eq. (10) admits the solution

$$b_k(t) = -\frac{N_{fk}}{\omega_k N_{kk}} \int_0^t f(\tau) \sin(\omega_k(t - \tau)) \, \mathrm{d}\tau \tag{11}$$

3. 3-D axisymmetric model

The 3-D axisymmetric model consists of two thin disks capping the two ends of a short cylinder (see Fig. 3(a)). The cylinder transfer matrix is derived in Section 3.1. Dynamic impedance of the disk at its boundary is derived in Section 3.2. Finally, the procedure of coupling motions of cylinder and disks is derived in Section 3.3.
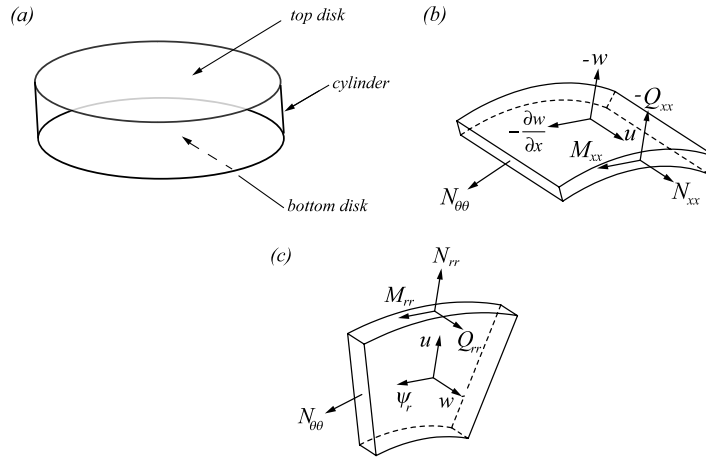
Fig. 3. 3-D axisymmetric model: (a) geometry, (b) cylinder element, (c) disk element.

3.1. Cylinder transfer matrix

The cylinder has radius a_c, length l_c, plate thickness h_c, modulus E_c, Poisson's ratio v_c, and mass density ρ_c. Forces and displacements of a cylinder element are shown in Fig. 3(b). For periodic motions in time with frequency ω, the coupled axisymmetric elasto-dynamic equations of the cylinder are

$$
\begin{aligned}
&\partial_x N_{xx} = -\rho_c h_c \omega^2 u_c \\
&\partial_x Q_x + \frac{N_{\theta\theta}}{a_c} = -\rho_c h_c \omega^2 w_c \\
&Q_x = \partial_x M_{xx} - \frac{\rho_c h_c^3}{12} \chi \omega^2 \partial_x w_c, \quad \chi = 1 + \frac{2\kappa}{1 - v_c}
\end{aligned}
\tag{12}
$$

(x, θ) are axial and circumferential coordinates, (u_c, w_c) are axial and radial displacement, the factor χ multiplying rotatory inertia accounts for shear deformation and κ is shear constant (El-Raheb and Wagner, 1989b), and (N_{xx}, Q_{xx}, M_{xx}) are axial, shear and moment resultants relating to displacements by the constitutive law

$$
\begin{aligned}
&N_{xx} = \frac{E_c h_c}{1 - v_c^2} \left[\partial_x u_c - v_c \frac{w_c}{a_c} \right] \\
&N_{\theta\theta} = \frac{E_c h_c}{1 - v_c^2} \left[v_c \partial_x u_c - \frac{w_c}{a_c} \right] \\
&M_{xx} = -\frac{E_c h_c^3}{12(1 - v_c^2)} \partial_{xx} w_c
\end{aligned}
\tag{13}
$$

Substituting (13) in (12) leads to a sixth order system of ordinary differential equations in (u_c, w_c)

$$
\mathbf{D}_c \begin{Bmatrix} u_c \\ w_c \end{Bmatrix} = \mathbf{0}
\tag{14}
$$

Since the operator $\mathbf{D}_c$ has constant coefficients, the solution is in terms of exponentials

$$\begin{Bmatrix} u_c(x) \\ w_c(x) \end{Bmatrix} = \begin{Bmatrix} u_{cj} \\ w_{cj} \end{Bmatrix} e^{\lambda_{cj}x} \tag{15}$$

Substituting (15) in (14) yields a homogeneous set of simultaneous equations

$$\mathbf{L}_c \begin{Bmatrix} u_c \\ w_c \end{Bmatrix} = \mathbf{0} \;\; \Rightarrow \;\; \det[\mathbf{L}_c] = 0 \tag{16a}$$

The implicit eigenvalue problem (16a) yields the eigenvalues λ_{cj}, eigenvectors $\{C_{cuj}, C_{cwj}\}^{\mathrm{T}}$, and solutions for u_c, w_c

$$u_c(x) = \sum_{j=1}^{6} C_{cuj} e^{\lambda_{cj}x}, \quad w_c(x) = \sum_{j=1}^{6} C_{cwj} e^{\lambda_{cj}x} \tag{16b}$$

Define the state vector $\mathbf{S}_c(x)$ as

$$\mathbf{S}_c(x) = \begin{Bmatrix} \mathbf{f}_c(x) \\ \mathbf{g}_c(x) \end{Bmatrix} \tag{17}$$

$$\mathbf{f}_c = \{N_{xx}, Q_{xx}, M_{xx}\}^{\mathrm{T}}, \quad \mathbf{g}_c = \{u_c, w_c, \partial_x w_c\}^{\mathrm{T}}$$

Substituting (16b) in (13) then in (17)

$$\mathbf{S}_c(x) = \mathbf{B}_c(x)\mathbf{C}_c, \quad \mathbf{C}_c = \{C_{cu1}, C_{cu2}, \ldots, C_{cw1}, C_{cw2}, \ldots\}^{\mathrm{T}} \tag{18}$$

$\mathbf{B}_c(x)$ is a matrix of exponentials. Evaluating (18) at the two boundaries of the cylinder $x = 0, l_c$ then eliminating $\mathbf{C}_c$

$$\mathbf{S}_c(l_c) = \mathbf{B}_c(l_c) \cdot \mathbf{B}_c^{-1}(0) \cdot \mathbf{S}_c(0) \equiv \mathbf{T}_c(0 \rightarrow l_c)\mathbf{S}_c(0) \tag{19a}$$

$\mathbf{T}_c(0 \rightarrow l_c)$ is the cylinder transfer matrix relating $\mathbf{S}_c$ at its two boundaries. Eq. (19a) can be expressed in terms of four sub-matrices

$$\begin{Bmatrix} \mathbf{f}_c(l_c) \\ \mathbf{g}_c(l_c) \end{Bmatrix} = \begin{bmatrix} \mathbf{t}_{c11} & \mathbf{t}_{c12} \\ \mathbf{t}_{c21} & \mathbf{t}_{c22} \end{bmatrix} \begin{Bmatrix} \mathbf{f}_c(0) \\ \mathbf{g}_c(0) \end{Bmatrix} \tag{19b}$$

3.2. Disk impedance matrix

Each disk has radius a_c which is the same as the cylinder's, plate thickness h_d, and modulus E_d, Poisson's ratio v_d and mass density ρ_d. Forces and displacements of a disk element are shown in Fig. 3(c). For periodic motions in time with frequency ω, the in-plane axisymmetric equation of the disk is

$$\partial_r N_{rr} + \frac{(N_{rr} - N_{\theta\theta})}{r} = \rho_d h_d \omega^2 u_d \tag{20}$$

(r, θ) are radial and circumferential coordinates, u_d is radial displacement, and $(N_{rr}, N_{\theta\theta})$ are radial and circumferential stress resultants relating to displacements by the constitutive law

$$N_{rr} = \frac{E_d h_d}{1 - v_d^2} \left[\partial_r u_d + v_d \frac{u_d}{r} \right]$$

$$N_{\theta\theta} = \frac{E_d h_d}{1 - v_d^2} \left[v_d \partial_r u_d + \frac{u_d}{r} \right] \tag{21}$$

Substituting (21) in (20) yields

$$[\nabla_1^2 + \rho_d h_d \omega^2] u_d = 0, \quad \nabla_n^2 \equiv \partial_{rr} + \frac{1}{r} \partial_r - \frac{n^2}{r} \tag{22}$$

with solution

$$u_d(r) = C_{du} J_1(k_{d\varepsilon} r)$$

$$k_{d\varepsilon} = \frac{\omega}{c_{d\varepsilon}}, \quad c_{d\varepsilon} = \sqrt{\frac{E_d}{(1 - v_d^2)\rho_d}} \tag{23}$$

Mindlin's axisymmetric flexural plate equations of the disk are (El-Raheb and Wagner, 2001)

$$\frac{\widetilde{D}}{2} \left[(1 - v_d)\nabla_1^2 \psi_d + (1 + v_d)\partial_{rr}\psi_d \right] - \kappa G_d h_d(\psi_d + \partial_r w_d) = -\frac{\rho_d h_d^3}{12} \omega^2 \psi_d$$

$$\kappa G_d h_d(\nabla^2 w_d + \partial_r \psi_d) = -\rho_d h_d \omega^2 w_d, \quad \widetilde{D} = \frac{E_d h_d^3}{12(1 - v_d^2)} \tag{24}$$

with constitutive relations

$$M_{rr} = \widetilde{D}\left(\partial_r \psi_d + v_d \frac{\psi_d}{r} \right), \quad Q_r = \kappa G_d h_d(\partial_r w_d + \psi_d) \tag{25}$$

w_d, ψ_d are axial displacement and rotation, Q_r, M_{rr} are shear and moment resultants, and κ is shear constant. Eliminating ψ_r in (24) yields the fourth order equation in w_d

$$\left[\left(\nabla_0^2 + \frac{\omega^2}{c_{d\varepsilon}^2} \right) \left(\nabla_0^2 + \frac{\omega^2}{c_{ds}^2} \right) - \frac{12\omega^2}{c_{d\varepsilon}^2 h_d^2} \right] w_d = 0, \quad c_{ds} = \sqrt{\frac{\kappa G_d}{\rho_d}} \tag{26}$$

with general solution in terms of Bessel functions

$$w_d(r) = C_{dw} J_0(\lambda_r r) \tag{27}$$

Substituting (27) in (26) yields the dispersion relation

$$(-\lambda_r^2 + k_{d\varepsilon}^2)(-\lambda_r^2 + k_{ds}^2) - \frac{12k_{d\varepsilon}^2}{h_d^2} = 0$$

$$k_{d\varepsilon} = \omega/c_{d\varepsilon}, \quad k_{ds} = \omega/c_{ds} \tag{28}$$

The four roots λ_{rj} of (28) correspond to four primitives where only the two regular at $r = 0$ are retained

$$w_d(r) = \sum_{j=1}^{2} C_{dwj} J_0(\lambda_{rj} r)$$

$$\psi_d(r) = \sum_{j=1}^{2} C_{d\psi j} J_0'(\lambda_{rj} r), \quad C_{d\psi j} = -\frac{1}{\lambda_{rj}}(\lambda_{rj}^2 + k_{rs}^2) C_{dwj} \tag{29}$$

( )$'$ is derivative with respect to the argument.

Define the state vector $\mathbf{S}_d$ combining in and out of the plane variables

$$\mathbf{S}_d = \{\mathbf{f}_d, \mathbf{g}_d\}^T$$

$$\mathbf{f}_d = \{N_{rr}, Q_r, M_{rr}\}^T, \quad \mathbf{g}_d = \{u_d, w_d, \psi_d\}^T \tag{30}$$

Substituting (23) and (29) in (21) and (25) yields

$$\mathbf{f}_d(r) = \mathbf{B}_{fd}(r)\mathbf{C}_d, \quad \mathbf{g}_d(r) = \mathbf{B}_{gd}(r)\mathbf{C}_d$$

$$\mathbf{C}_d = \mathbf{B}_{gd}^{-1}(a_c)\mathbf{g}_d(a_c), \quad \mathbf{C}_d = \{C_{du}, C_{dw1}, C_{dw2}\}^{\mathrm{T}} \tag{31}$$

$\mathbf{B}_{fd}$ and $\mathbf{B}_{gd}$ are 3×3 matrices. Eliminating $\mathbf{C}_d$ from (31) determines the disk impedance matrix

$$\mathbf{f}_d(r) = \mathbf{B}_{fd}(r)\mathbf{B}_{gd}^{-1}(r)\mathbf{g}(r) \equiv \mathbf{Z}_d(r)\mathbf{g}_d(r) \tag{32}$$

$\mathbf{Z}_d(a_c) = \mathbf{B}_{fd}(a_c) \cdot \mathbf{B}_{gd}^{-1}(a_c)$ is the impedance matrix of the disk at the boundary.

3.3. Coupling cylinder and disks

Continuity of $\mathbf{S}$ at the cylinder-disk interface $x = x_e \equiv 0, l_c$ and $r = a_c$ requires expressing $\{\mathbf{f}_d, \mathbf{g}_d\}$ in the coordinate system of $\{\mathbf{f}_c, \mathbf{g}_c\}$ by means of a re-ordering matrix

$$\mathbf{f}_c(x_e) = \mathbf{R}_f\mathbf{f}_d(a_c), \quad \mathbf{g}_c(x_e) = -\mathbf{R}_f\mathbf{g}_d(a_c) \;\Rightarrow\; \mathbf{g}_d(a_c) = -\mathbf{R}_f^{-1}\mathbf{g}_c(x_e)$$

$$\mathbf{R}_f = \begin{bmatrix} 0 & -1 & 0 \\ 1 & 0 & 0 \\ 0 & 0 & -1 \end{bmatrix} \tag{33}$$

Substituting (32) in (33) then eliminating $\mathbf{g}_d$

$$\mathbf{f}_c(0) = \mathbf{Z}_c\mathbf{g}_c(0), \quad \mathbf{f}_c(l_c) = -\mathbf{Z}_c\mathbf{g}_c(l_c)$$

$$\mathbf{Z}_c = -\mathbf{R}_f\mathbf{Z}_d(a_c)\mathbf{R}_f^{-1} \tag{34}$$

$\mathbf{Z}_c$ is disk impedance in the cylinder coordinate system. Applying (34) at the two boundaries of the cylinder and relating $\mathbf{f}_c(l_c)$, $\mathbf{g}_c(l_c)$ to $\mathbf{f}_c(0)$, $\mathbf{g}_c(0)$ using (19b) produces the homogeneous equations

$$\mathbf{M}_c\begin{Bmatrix} \mathbf{S}_c(0) \\ \mathbf{S}_c(l_c) \end{Bmatrix} = \begin{Bmatrix} \mathbf{0} \\ \mathbf{0} \end{Bmatrix}, \quad \mathbf{M}_c = \begin{bmatrix} \mathbf{I} & -\mathbf{Z}_c & \mathbf{O} & \mathbf{O} \\ \mathbf{t}_{c11} & \mathbf{t}_{c12} & -\mathbf{I} & \mathbf{O} \\ \mathbf{t}_{c21} & \mathbf{t}_{c22} & \mathbf{O} & -\mathbf{I} \\ \mathbf{O} & \mathbf{O} & \mathbf{I} & \mathbf{Z}_c \end{bmatrix} \tag{35}$$

$\mathbf{M}_c$ is a 12×12 matrix, $\mathbf{I}$ and $\mathbf{O}$ are 3×3 unit and null matrices, and $\mathbf{0}$ is the null vector of order 6. A non-trivial solution of (35) yields the implicit eigenproblem

$$\det[\mathbf{M}_c] = 0 \;\Rightarrow\; \{\mathbf{\Phi}_c, \boldsymbol{\omega}\}_k \tag{36a}$$

Eqs. (31) and (33) determine the disk eigenfunction $\mathbf{\Phi}_d(r)$. The global eigenfunction of cylinder and conjoined disks then follows:

$$\mathbf{\Phi}_{Gk}(s) = \{\mathbf{\Phi}_c(x), \mathbf{\Phi}_d(r)\}_k^{\mathrm{T}} \tag{36b}$$

s is an intrinsic coordinate along the boundary; $s \equiv x$ on the cylinder and $s \equiv r$ on the disks. Modal analysis proceeds by expanding the global displacement vector $\mathbf{g}_G(s, t) = \{\mathbf{g}_c(x), \mathbf{g}_d(r)\}^{\mathrm{T}}$ in terms of the orthogonal set (36b)

$$\mathbf{g}_G(s, t) = \sum_k b_k(t)\mathbf{\Phi}_{Gk}(s) \tag{37}$$

Substituting (37) in the forced elasto-dynamic equations of motion of cylinder and disks and enforcing orthogonality of the $\{\mathbf{\Phi}_{Gk}(s)\}$ set yields uncoupled ordinary differential equations in $b_k(t)$

$$\ddot{b}_k(t) + \omega_k^2 b_k(t) = N_{fk}f(t)/N_{kk}$$

$$N_{fk} = \langle \mathbf{p}(s)|\rho\mathbf{\Phi}_{Gk}(s)\rangle, \quad N_{kk} = \langle \mathbf{\Phi}_{Gk}(s)|\rho\mathbf{\Phi}_{Gk}(s)\rangle \tag{38}$$

(˙) is time derivative, $\mathbf{p}(s)$ is spatial vector of external excitation, $f(t)$ is its time dependence, and ρ is density. Eq. (38) admits the solution

$$b_k(t) = -\frac{N_{fk}}{\omega_k N_{kk}} \int_0^t f(\tau) \sin(\omega_k(t-\tau)) \, \mathrm{d}\tau \tag{39}$$

For frequency response, $\ddot{b}_k(t) = -\omega^2 b_{k0} \mathrm{e}^{\mathrm{i}\omega t}$ reducing (38) to

$$b_k(t) = N_{fk}\mathrm{e}^{\mathrm{i}\omega t}/(N_{kk}(-\omega^2 + \omega_k^2)) \tag{40}$$

ω is frequency of excitation.

4. Forcing pressure

In the 3-D axisymmetric model, a spatial distribution of the applied pressure is approximated by the bell-shaped function

$$p(r) = p_0 + p_1 \operatorname{sech}(p_2 r), \quad 0 \leqslant r \leqslant a_c \tag{41}$$

where the triad (p_0, p_1, p_2) of constants characterizes translation, magnification and maximum slope of the profile. Different triads are assigned to top and bottom disks (see Fig. 3(a)). A typical normalized distribution is shown in Fig. 4.

In the 2-D model, assuming that pressure acts over a distance l_x along z where l_x is length of capsule along top or bottom faces (see Fig. 2(a)), a profile similar to (41) is used but with p_0, p_1 scaled to conserve total force

$$\tilde{p}(x) = \tilde{p}_0 + \tilde{p}_1 \operatorname{sech}(p_2(x - 0.5l_x)), \quad 0 \leqslant x \leqslant l_x \tag{42}$$

The condition of force conservation yields

$$l_x \int_0^{l_x} \tilde{p}(x) \, \mathrm{d}x = 2\pi \int_0^{a_c} p(r) r \, \mathrm{d}r, \quad l_x = 2a_c \tag{43}$$

Assuming that $p_0/p_1 = \tilde{p}_0/\tilde{p}_1$, then Eq. (43) suffices to determine the dyad $(\tilde{p}_0, \tilde{p}_1)$.
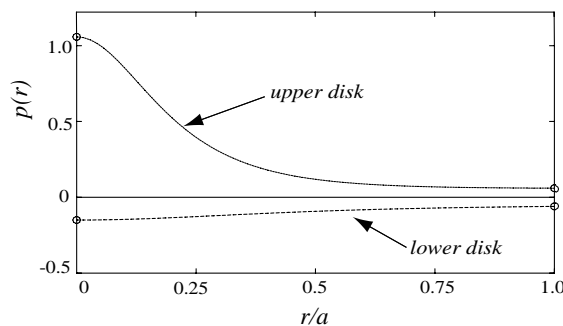

Fig. 4. Radial distribution of internal pressure $p(r) = p_0 + p_1 \operatorname{sech}(p_2 r)$.

5. Dynamic mobility

Mobility Y_n along a unit vector **n** normal to the boundary relates pressure p to pressure gradient $\partial_n p$ at that boundary

$$\partial_n p = Y_n p \tag{44}$$

Since comminuted material has no shear rigidity, it can be considered a fluid where the acoustic equation applies. Pressure gradient $\partial_n p$ is then related to acceleration $\partial_{tt} u_n$ by the momentum equation

$$(1/\rho_f)\partial_n p = \partial_{tt} u_n \tag{45}$$

ρ_f is fluid density and u_n is acoustic displacement along **n**. Substituting (44) in (45) yields

$$Y_n p = \rho_f \partial_{tt} u_n \tag{46}$$

Y_n's dimension is 1/length. For frequency response with frequency ω

$$\rho_f \partial_{tt} u_n(s,t) \equiv -\rho_f \bar{u}_n(s,\omega)\omega^2 \mathrm{e}^{\mathrm{i}\omega t} = -Y_n(s,\omega)\bar{p}(s,\omega)\mathrm{e}^{\mathrm{i}\omega t} \;\; \Rightarrow \;\; Y_n(s,\omega) = \rho_f \omega^2 \bar{u}_n(s,\omega)/\bar{p}(s,\omega) \tag{47}$$

To determine $Y_n(s,\omega)$, proceed through the following steps:

(a) For each disk capping the capsule, $Y_n \equiv Y_z$. Divide the disk into n_r ring segments of equal width $r_{k+1} - r_k = d_r \equiv r_d/n_r$, $1 \leqslant k \leqslant n_r$, where $r_1 = 0$ and $r_{n_r} = a_d$.
(b) On each ring termed the source segment, apply a uniform pressure of unit intensity.
(c) From Eqs. (37) and (40) compute the acceleration response $\omega^2 u_{zl,k}$ at the central line $r_{cl} = (r_{l+1} + r_l)/2$ of the lth segment termed the target line, from the kth source segment.

In Eq. (47), a $\bar{p}(s,\omega) = 1$ yields $Y_{zl,k}(s,\omega) = \rho_f \omega^2 u_{zl,k}(s,\omega)$.

6. Results

The 2-D capsule has a rectangular cross-section made of four plates as shown in Fig. 5:

(1) top plate joining corners 1 through 5
(2) bottom plate joining corners 6 through 10
(3) left plate joining corners 1 and 10
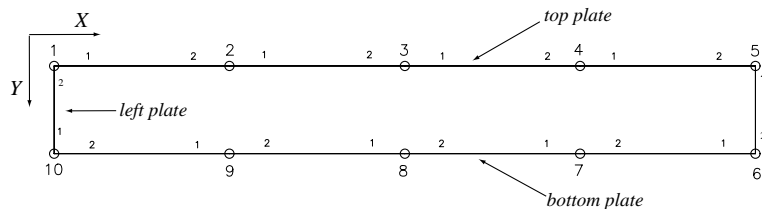(4) right plate joining corners 5 and 6

Fig. 5. Cross-section of 2-D capsule with corner and branch numbers.

A global coordinate system is defined for both the 2-D and 3-D models with origin at corner 1 such that $\{X : 0 \leqslant X \leqslant l_x\} \otimes \{Y : 0 \leqslant Y \leqslant w_y\}$ where (l_x, w_y) are length and width of the capsule. The following geometry and material properties are considered

$$l_x = 100 \text{ mm}, \quad w_y = 12.5 \text{ mm}, \quad h = 2.54 \text{ mm}$$

$$E = 2 \times 10^{12} \text{ dyn/cm}^2, \quad \rho = 8 \text{ g/cm}^3, \quad v = 0.3$$

where h is uniform plate thickness and (E, ρ, v) are Young's modulus, density and Poisson's ratio. In the 2-D model, three stresses are monitored along each segment's local x-axis: flexural stress σ_{xxf}, shear stress τ_{xz} and extensional axial stress σ_{xxe}. In the 3-D model four stresses are monitored; either $\sigma_{xxf}, \tau_{xz}, \sigma_{xxe}, \sigma_{\theta\theta e}$ along the cylinders x-axis which is the global Y-axis, where $\sigma_{\theta\theta e}$ is the extensional circumferential stress, or else $\sigma_{rrf}, \tau_{rz}, \sigma_{rre}, \sigma_{\theta\theta e}$ along the disk's radius which is the global X-axis. Stress at a point with global coordinates (X, Y) will be referred to as $\sigma(X, Y)$.

The first 10 mode shapes and corresponding resonant frequencies are shown in Fig. 6(a)–(j). The fundamental at 1.063 kHz (Fig. 6(a)) is symmetric about the axis of bilateral symmetry. This corresponds to the first symmetric flexural mode of the two faces. The second mode (Fig. 6(b)) is the first anti-symmetric flexural mode of the faces. Higher flexural modes with larger wave numbers are shown in Fig. 6(c)–(f) and then the fundamental symmetric extensional mode at 21.72 kHz (Fig. 6(g)), followed by the first anti-symmetric extensional mode (Fig. 6(h)) at 24.54 kHz. At higher frequencies (Fig. 6(i)–(j)), the flexural modes exhibit noticeable motion of the side plates, which were evanescent for frequencies below the fundamental symmetric extensional mode in Fig. 6(g). For each plate, modes belong to one of four groups depending on symmetry of the mode (symmetric or anti-symmetric) and type of mode (flexural or extensional).

In the 3-D axisymmetric model, a spatial distribution of the applied pressure on top and bottom plates is approximated by the bell-shaped function in Eq. (38) where the triad of constants (p_0, p_1, p_2) characterizes translation, magnification and maximum normalized slope of the profile. Different triads are assigned to top and bottom plates (see Fig. 4). The normalized peak pressure for the axisymmetric excitation is unity. In the 2-D model, the equivalent bell-shaped distribution with $(\tilde{p}_0, \tilde{p}_1)$ that conserves total force is
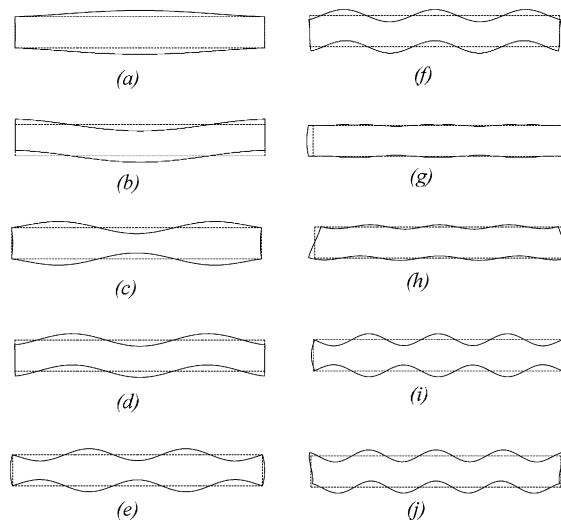

Fig. 6. Resonant frequencies and modes of 2-D capsule: (a) $\Omega = 1.063$ kHz; (b) $\Omega = 1.907$ kHz; (c) $\Omega = 5.941$ kHz; (d) $\Omega = 7.627$ kHz; (e) $\Omega = 14.737$ kHz; (f) $\Omega = 16.974$ kHz; (g) $\Omega = 21.724$ kHz; (h) $\Omega = 24.545$ kHz; (i) $\Omega = 27.252$ kHz; (j) $\Omega = 30.596$ kHz.

Table 1
Parameters of pressure profile

Plate	3-D model		2-D model		
	p_0	p_1	$\tilde{p}_0$	$\tilde{p}_1$	p_2
Top	0.06	1.0	0.0223	0.371	3.5
Bottom	0.05	0.1	0.0325	0.065	1.5
Side	0.039	0	0.039	0	0

determined applying Eq. (43). The resulting $(\tilde{p}_0, \tilde{p}_1)$ is listed in Table 1 showing that in the 2-D model, peak applied pressure on the top plate is $p_{mx} \equiv \tilde{p}_0 + \tilde{p}_1 = 0.4$. The top plate is divided into four equidistant intervals of 12.5 mm along X while the side plate is divided into two equidistant intervals of 6.25 mm along Y. The time dependence of the pressure pulse is trapezoidal lasting 25 μs with 5 μs rise and fall times and a 15 μs plateau.

Fig. 7 plots stress histories on the left plate for $0 \leqslant Y \leqslant 12.5$ mm. The peak of $\sigma_{xxf}(0,0)$ reaches $38p_{mx}$ (Fig. 7(a)) pointing to a location where material may yield and ultimately fail. σ_{xxe} (Fig. 7(c)) is relatively small since it reacts to the difference between integrated pressure over the top plate ($\approx p_{mx}l_x/4 \equiv O(1)$) and its inertia. Fig. 8 plots stress histories on the top plate for $12.5 \leqslant X \leqslant 50$ mm at 12.5 mm intervals. The peak of $\sigma_{xxf}(50,0)$ (Fig. 8(a)) reaches $23p_{mx}$ pointing to another location of considerable flexural stress. Fig. 8(b)
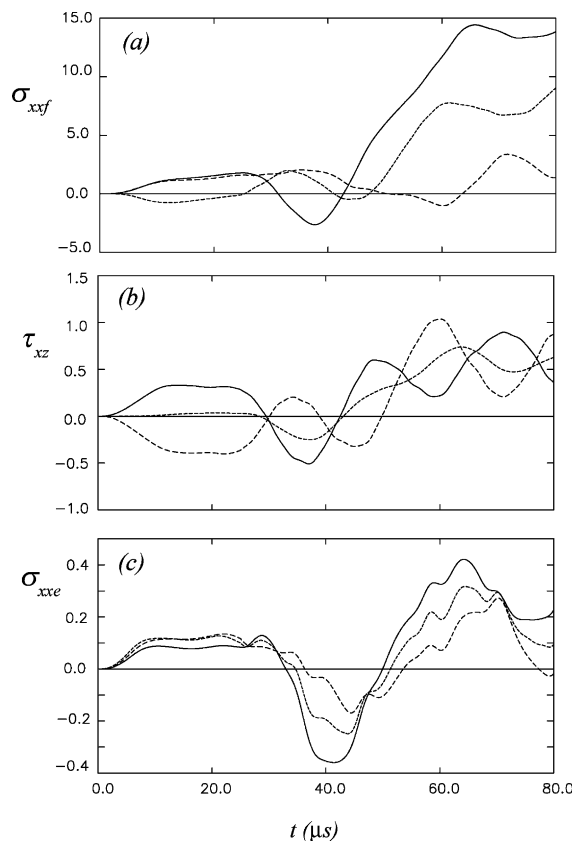

Fig. 7. 2-D stress histories on left plate: (a) σ_{xxf}, (b) τ_{xz}, (c) σ_{xxe}. (——) $Y = 0$, (– –) $Y = w_y/2$, (····) $Y = w_y$.
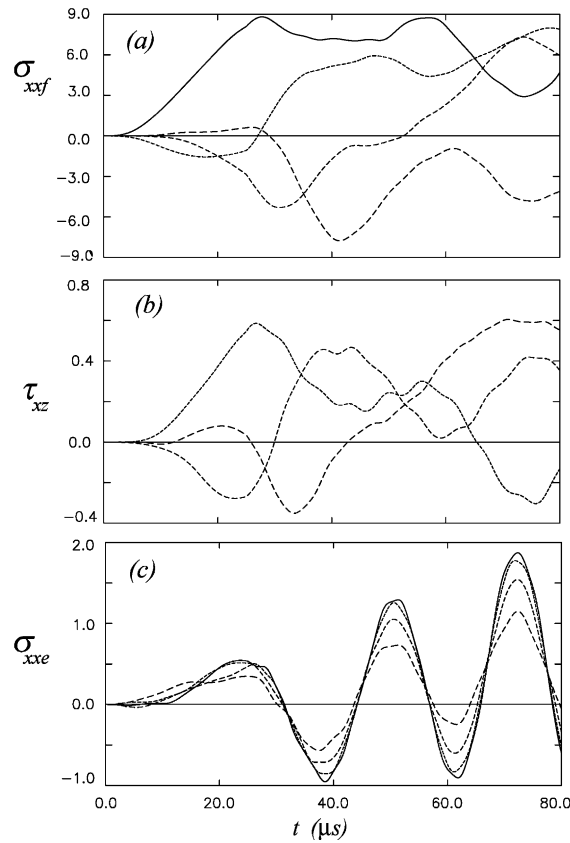
Fig. 8. 2-D stress histories on top plate: (a) σ_{xxf}, (b) τ_{xz}, (c) σ_{xxe}. (—) $X = 0.5l_x$, (- -) $X = 0.375l_x$, (·-·) $X = 0.25l_x$, (···) $X = 0.125l_x$.

plots histories of shear stress τ_{xz} with peaks not exceeding p_{mx}. Fig. 8(c) plots histories of extensional stress σ_{xxe} in the plane of the plate with a peak of $\sigma_{xxe}(50, 0)$ reaching $5p_{mx}$. It is evident that the two most vulnerable locations with high σ_{xxf} are at the interface of top and side plates and at the top plate's center. Extensional and shear stresses do not contribute to yielding and failure of the material unless deformation is sufficient to promote additional stress from nonlinear stretching.

Geometry and material properties in the 3-D model replicate those in the 2-D model. The first six mode shapes are plotted in the left column of Fig. 9 while the corresponding modes from the 2-D model are plotted in the right column for comparison. The fundamental mode 1 at 2.075 kHz is the first symmetric flexural mode of the disks while mode 2 at 4.714 kHz is the first anti-symmetric. Flexural modes 3, 4 and 6 then occur before the fundamental symmetric extensional mode 5 occurs at 29.74 kHz. The frequency ratio $\omega_{3\text{-D}}/\omega_{2\text{-D}}$ for modes 1, 2 and 4 is approximately 2 (Fig. 9). This ratio drops to less than 1.3 for all following modes suggesting that the difference in response between 3-D and 2-D models is largest at low frequencies. It also implies that for a pulse of short duration compared to the fundamental period, transient response from the two models may be comparable since then response would be controlled by modes with short wavelength.

Fig. 10 plots stress histories on the cylinder for $0 \leqslant Y \leqslant 12.5$ mm. The peak of $\sigma_{xxf}(0, 0)$ (Fig. 10(a)) is half that in 2-D while the peak of σ_{xxe} (Fig. 10(c)) is almost the same as that in 2-D. $\sigma_{\theta\theta e}$ (Fig. 10(d)) is approximately $1/4\sigma_{xxf}$ and has no counterpart in 2-D. Fig. 11 plots stress histories on the top disk for $0 \leqslant X \leqslant 50$ mm at 12.5 mm intervals. The peak of $\sigma_{rrf}(50, 0)$ reaches the same magnitude as that of $\sigma_{xxf}(0, 0)$
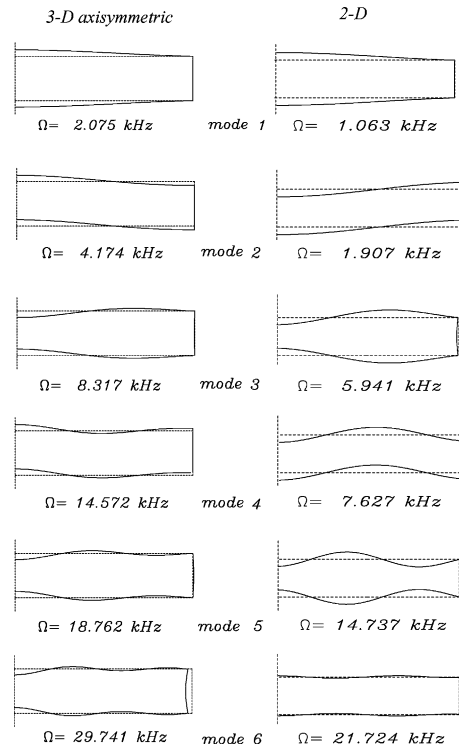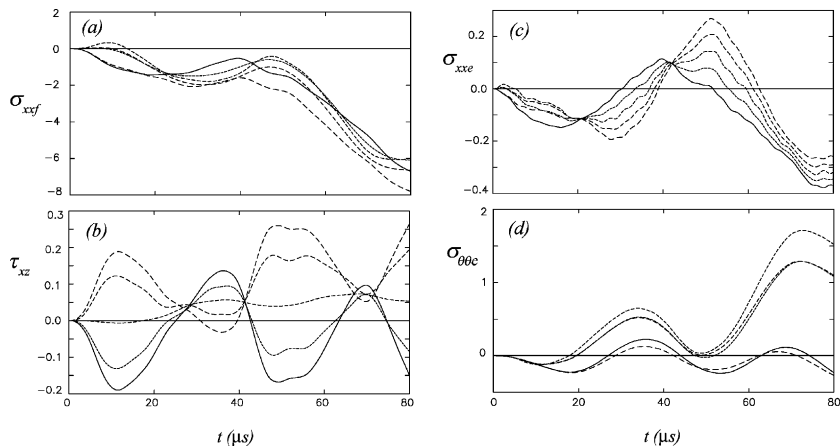
Fig. 9. Comparison of modes from 3-D axisymmetric and 2-D models.

Fig. 10. 3-D stress histories on cylinder: (a) σ_{xxf}, (b) τ_{xz}, (c) σ_{xxe}, (d) $\sigma_{\theta\theta c}$. (—) $Y = 0$, (---) $Y = 0.25w_y$, (····) $Y = 0.5w_y$, (···) $Y = 0.75w_y$, (··) $Y = w_y$.

in 2-D, and the peak of $\sigma_{rrf}(0,0)$ reaches the same magnitude as that of $\sigma_{xxf}(50,0)$ in 2-D. Fig. 11(b) plots histories of shear stress τ_{xz} with a peak 1/3 that in 2-D. σ_{rre} and $\sigma_{\theta\theta e}$ (Fig. 11(c), (d)) have approximately the same magnitude reaching 1/5 that of σ_{xxe} in 2-D. Consequently in 3-D, magnitude of peak flexural stress is
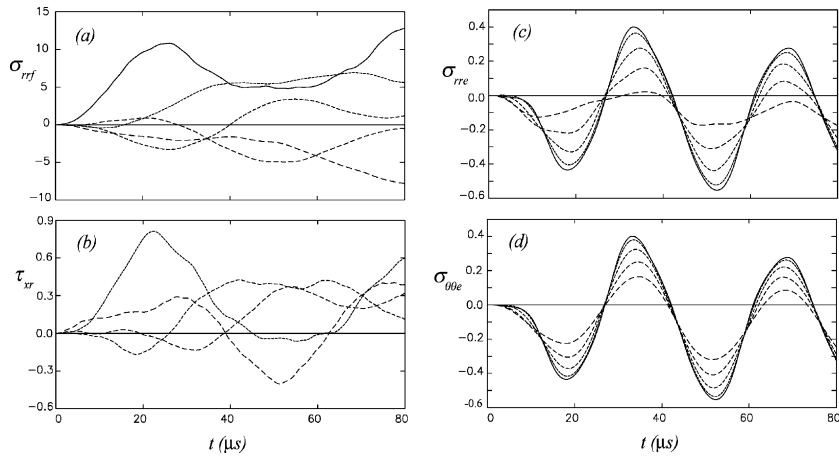
Fig. 11. 3-D stress histories on top disk: (a) σ_{rrf}, (b) τ_{xr}, (c) σ_{rre}, (d) $\sigma_{\theta\theta e}$. (——) $X = 0.5l_x$, (——) $X = 0.375l_x$, (----) $X = 0.25l_x$, (····) $X = 0.125l_x$, (··) $X = 0$.

approximately the same as in 2-D but locations are reversed; highest stress is at the disk's center followed by that at the edge. It is surprising that in spite of the different dimensionality, histories of flexural stress from the two models agree qualitatively and quantitatively. The discrepancy between the two models is in the extensional stress that is substantially lower than flexural stress.

Fig. 12 follows the evolution of deformation of the 3-D capsule for $10 \leqslant t \leqslant 80$ µs. The dominant mode of deformation is a symmetric bulging that is larger on the top plate than on the bottom due to the difference in magnitude of the applied pressure.

Fig. 13 plots frequency response of driving point acceleration mobility $\log_{10} |M_{z\omega}| = \log_{10} |\omega^2 u_{zl,l}|$ for a titanium capsule at four stations along the disk's radius $r_{cl} = 0, 0.25a_d, 0.5a_d, 0.75a_d$. Resonant peaks are attenuated by a modal damping coefficient $\zeta = 0.08$ independent of frequency. In this way, only average response is retained. Clearly, $M_{z\omega}$ vanishes at $\omega = 0$, exhibits sharp peaks and valleys at low frequency where modal damping is not effective then reaches an almost constant plateau for large ω. The plateau level is almost independent of position along the disk radius. The frequency-averaged driving point mobility $Y_\omega(s)$ defined by
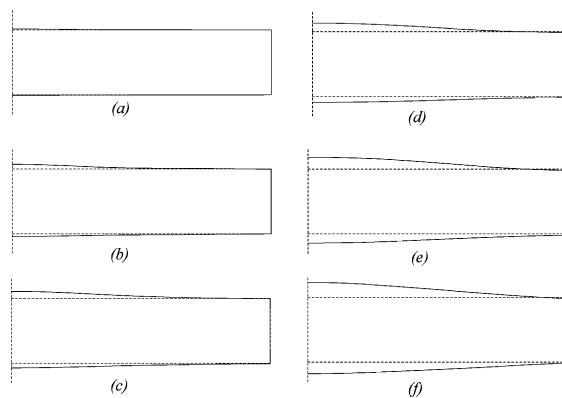

Fig. 12. Time snapshots of 3-D capsule: (a) $t = 10$ µs; (b) $t = 20$ µs; (c) $t = 30$ µs; (d) $t = 40$ µs; (e) $t = 60$ µs; (f) $t = 80$ µs.
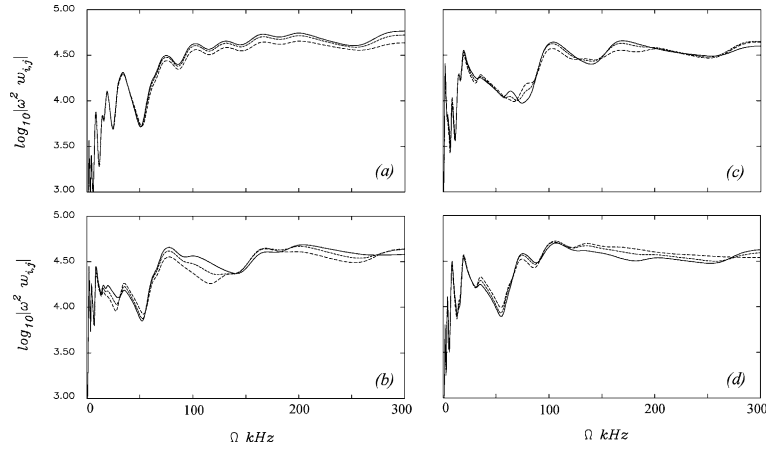
Fig. 13. Driving point acceleration mobility from ring loads on disk ring load at: (a) $r_{cl}/a_d = 0$, (b) $r_{cl}/a_d = 0.25$, (c) $r_{cl}/a_d = 0.5$, (d) $r_{cl}/a_d = 0.75$. (—) element "$i - 1$", (—) element "i", (····) element "$i + 1$".
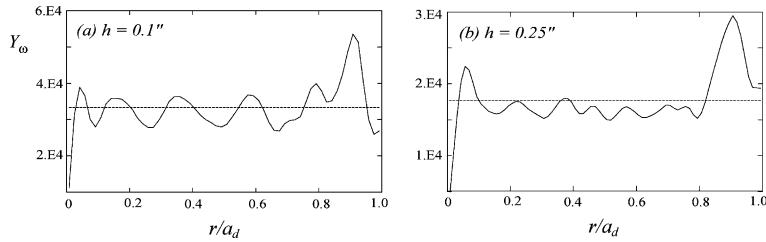

Fig. 14. Distribution of frequency-averaged acceleration mobility from ring load, (a) $h = 0.1$ in., (b) $h = 0.25$ in.

$$Y_\omega(s) = \frac{1}{\omega_{ub}} \int_0^{\omega_{ub}} |\omega^2 u_n(s, \omega)| \, d\omega \simeq \frac{1}{N_\omega} \sum_{j=1}^{N_\omega} |\omega_j^2, u_n(s, \omega_j)| \tag{48}$$

ω_{ub} is the highest frequency in the truncated modal expansion and N_ω is the number of frequencies sampled in the frequency response of Fig. 13. Fig. 14(a) and (b) plots $Y_\omega(r_{cl})$ versus r_{cl}/a_d for a 2.54 mm thick steel capsule and for a 6.35 mm thick Titanium capsule. The dashed line is the average $Y_\omega(r_{cl})$ over the radius. Since $\bar{p}(s, \omega) = 1$, a frequency independent approximation to Y_z is

$$Y_z \approx \rho_f [\omega^2 \bar{u}_z(s, \omega)]_{av} = \rho_f Y_{\omega av} \tag{49}$$

For the 0.25 in. thick titanium capsule $Y_z \approx 2 \text{ cm}^{-1}$.

7. Conclusion

Two models are presented for transient response of a thin walled capsule forced by a time dependent internal pressure. The 2-D model has finite dimensions in the plane of the cross-section and extends to infinity normal to this plane. The 3-D axisymmetric model includes a short thin cylinder capped by two thin disks. Both models adopt transfer matrices relating state variables at two ends of a segment and transient response based on modal analysis. Noteworthy results are

(1) For low wave numbers, eigenfrequencies of the 3-D model are twice those of the 2-D model. The difference diminishes as wave number rises.
(2) The assumed bell-shaped internal pressure distribution agrees with that determined from an acoustic model and from a numerical general purpose program.
(3) In both the 2-D and 3-D models, peak flexural stress occurs at the junction of cylinder and disks as well as center of disks.
(4) Peak extensional and shear stresses are one order of magnitude smaller than peak flexural stress except for circumferential stress in the cylinder with peak 1/4 that of flexural stress.
(5) In spite of the different dimensionality, histories from the two models are in good agreement.
(6) Frequency response of driving point mobility exhibits a plateau at high frequencies with magnitude independent of position in the capsule. In a frequency range bounded by the highest eigenfrequency of the truncated set, frequency-averaged mobility is almost constant along disk radius.

Appendix A. Transfer matrix of 2-D strip

For sinusoidal time dependence with frequency ω, the linear elasto-dynamic equations of a 2-D strip are

$$
\begin{aligned}
&\frac{\partial^2 u_s}{\partial x^2} = -k_{s\varepsilon}^2 u_s, \quad k_{s\varepsilon} = \omega/c_{s\varepsilon}, \quad c_{s\varepsilon} = \sqrt{E_s/\rho_s(1 - v_s^2)} \\
&\widetilde{D}\frac{\partial^2 \psi_s}{\partial x^2} - \kappa G_s h_s\left(\psi_s + \frac{\partial w_s}{\partial x}\right) = -\frac{\rho_s h_s^3}{12}\omega^2 \psi_s \\
&\kappa G_s h_s\left(\frac{\partial^2 w_s}{\partial x^2} + \frac{\partial \psi_s}{\partial x}\right) = -\rho_s h_s \omega^2 w_s, \quad \widetilde{D} = \frac{E_s h_s^3}{12(1 - v_s^2)}
\end{aligned}
\tag{A.1}
$$

u_s, w_s, ψ_s are displacements along local coordinates x and y (see Fig. 1(c)), E_s, G_s, v_s, ρ_s are extensional and shear moduli, Poisson's ratio, and mass density, h_s is thickness and κ is shear constant. The corresponding constitutive relations are

$$
\begin{aligned}
&f_x = \frac{E_s h_s}{(1 - v_s^2)}\frac{\partial u_s}{\partial x} \\
&q_x = \kappa G_s h_s\left(\frac{\partial w_s}{\partial x} + \psi_s\right), \quad m_x = \widetilde{D}\frac{\partial \psi_s}{\partial x}
\end{aligned}
\tag{A.2}
$$

f_x, q_x, m_x are axial force, shear force and moment (see Fig. 1(c)). The general solution of (A.1) takes the form

$$
\begin{Bmatrix} u_s(x) \\ w_s(x) \\ \psi_s(x) \end{Bmatrix} =
\begin{bmatrix}
e^{k_{s\varepsilon}x} & 0 & 0 \\
0 & e^{\lambda_{s1}x} & e^{\lambda_{s2}x} \\
0 & \delta_{s1}e^{\lambda_{s1}x} & \delta_{s2}e^{\lambda_{s2}x}
\end{bmatrix}
\begin{Bmatrix} C_{su} \\ C_{sw1} \\ C_{sw2} \end{Bmatrix}, \quad
\delta_{sj} = -\frac{1}{\lambda_{sj}}(\lambda_{sj}^2 + k_{ss}^2)
\tag{A.3}
$$

$\lambda_{s1,2}$ satisfy the dispersion relation

$$
\begin{aligned}
&(-\lambda_{sj}^2 + k_{s\varepsilon}^2)(-\lambda_{sj}^2 + k_{ss}^2) - \frac{12k_{s\varepsilon}^2}{h_s^2} = 0 \\
&k_{ss} = \omega/c_{ss}, \quad c_{ss} = \sqrt{\kappa G_s/\rho_s}
\end{aligned}
\tag{A.4}
$$

Substituting (A.4) in (A.2) in terms of the state vector $\mathbf{S}_s = \{\mathbf{f}_s, \mathbf{g}_s\}^T$

$$
\begin{aligned}
&\mathbf{S}_s(x) = \mathbf{B}_s(x)\mathbf{C}_s \\
&\mathbf{f}_s = \{f_x, q_x, m_x\}_s^T, \quad \mathbf{g}_s = \{u, w, \psi\}_s^T
\end{aligned}
\tag{A.5}
$$

$\mathbf{B}_s(x)$ is a 3×3 matrix of exponentials and $\mathbf{C}_s = \{C_{su}, C_{sw1}, C_{sw2}\}^{\mathrm{T}}$. Evaluating (A.5) at the two ends of the strip $(0, l_s)$ then eliminating $\mathbf{C}_s$ yields the strip's transfer matrix

$$\mathbf{S}_s(l_s) = \mathbf{B}_s(l_s)\mathbf{B}_s^{-1}(0)\mathbf{S}_s(0) = \mathbf{T}_s(0 \to l_s)\mathbf{S}_s(0) \tag{A.6}$$

References

El-Raheb, M., Wagner, P., 1985. Harmonic response of cylindrical and toroidal shells enclosing an acoustic medium, Part I: Theory. Journal of the Acoustical Society of America 78, 738–746.

El-Raheb, M., Wagner, P., 1986. Damped response of shells with vibration absorbers. Journal of Applied Mechanics Transactions of American Society of Mechanical Engineers 53, 902–908.

El-Raheb, M., Wagner, P., 1987. Wave propagation in a plate after impact by a projectile. Journal of the Acoustical Society of America 82, 498–505.

El-Raheb, M., Wagner, P., 1989a. Wave propagation in thin cylinders with point masses. Journal of the Acoustical Society of America 85, 759–767.

El-Raheb, M., Wagner, P., 1989b. Acoustic radiation from a shell with internal structures. Journal of the Acoustical Society of America 85, 2452–2464.

El-Raheb, M., Wagner, P., 1994a. Transient waves in a thick disc. Journal of the Acoustical Society of America 95, 3287–3299.

El-Raheb, M., 1994b. Flexural waves in a disk soon after impact. Journal of the Acoustical Society of America 96, 221–234.

El-Raheb, M., 1997. Simplified models of transient uniaxial waves in a layered periodic stack. International Journal of Solids and Structures 34, 2969–2990.

El-Raheb, M., Wagner, P., 2001. Transient flexural waves in a disk and square plate from off-center impact. Journal of the Acoustical Society of America 110, 2991–3002.

Karunasena, W., Wang, C., Kitipornchai, S., Xiang, Y., 1997. Exact solutions for axisymmetric bending of continuous annular plates. Computers and Structures 63, 455–464.

Liew, K., Yang, B., 2000. Elasticity solutions for free vibrations of annular plates from three-dimensional analysis. International Journal of Solids and Structures 37, 7689–7702.

Lin, C., Jen, M., 2003. Analysis of laminated anisotropic cylindrical shell by Chebyshev collocation method. Journal of Applied Mechanics Transactions of American Society of Mechanical Engineers 70, 391.

Soamidas, V., Ganesan, N., 1991. Vibration analysis of thick, polar orthotropic, variable thickness annular disks. Journal of Sound and Vibration 147, 39–56.

Um, C., Liew, K., Kitipornchai, S., 1998. Vibration of open cylindrical shells: a three-dimensional elasticity approach. Journal of the Acoustical Society of America 104, 1436.

Wang, C., Swaddiwudhipong, S., Tian, J., 1997. Ritz method for vibration analysis of cylindrical shells with ring stiffeners. Journal of Engineering Mechanics 123, 134.

Weber K., Hohler V., 1997. Protection efficiency of layered Aluminum Nitride ceramic targets bonded with Polyurethane films. Fraunhofer Institute Kurtzzeitdynamik, Ernst-Mach-Institut, Internal Report E-19/97.

Weber, K., El-Raheb, M., Hohler, V., 1999. Experimental investigations on the ballistic performance of layered AlN ceramic stacks. In: Proceedings of the 18th International Symposium on Ballistics, San Antonio, TX.

Xiang, Y., Liew, K., Kitipornchai, S.K., 1996. Vibration of circular and annular Mindlin plates with internal ring stiffeners. Journal of the Acoustical Society of America 100, 3696–3705.